Self-organized titanium oxide nano-channels for resistive memory application

A. Barman, C. P. Saini, P. Sarkar, B. Satpati, S. R. Bhattacharyya, D. Kabiraj, D. Kanjilal, S. Dhar, and A. Kanjilal

Citation: J. Appl. Phys. **118**, 224903 (2015); doi: 10.1063/1.4936961
View online: http://dx.doi.org/10.1063/1.4936961
View Table of Contents: http://aip.scitation.org/toc/jap/118/22
Published by the American Institute of Physics

AIP | Journal of Applied Physics
INTRODUCING INVITED PERSPECTIVES
Ultrafast magnetism and THz spintronics
Authors: Jakob Walowski and Markus Münzenberg

RIGHTSLINK

JOURNAL OF APPLIED PHYSICS **118**, 224903 (2015)

CrossMark click for updates

Self-organized titanium oxide nano-channels for resistive memory application

A. Barman,[1] C. P. Saini,[1] P. Sarkar,[2] B. Satpati,[3] S. R. Bhattacharyya,[3] D. Kabiraj,[4] D. Kanjilal,[4] S. Dhar,[1] and A. Kanjilal[1,a)]

[1]*Department of Physics, School of Natural Sciences, Shiv Nadar University, NH-91, Tehsil Dadri, Gautam Buddha Nagar, Uttar Pradesh 201 314, India*

[2]*Department of Physics, National Institute of Technology, Silchar, Assam 788 010, India*

[3]*Surface Physics and Material Science Division, Saha Institute of Nuclear Physics, 1/AF Bidhannagar, Kolkata 700 064, India*

[4]*Inter-University Accelerator Centre, Aruna Asaf Ali Marg, New Delhi 110 067, India*

(Received 9 October 2015; accepted 19 November 2015; published online 8 December 2015)

Towards developing next generation scalable TiO_2-based resistive switching (RS) memory devices, the efficacy of 50 keV Ar^+-ion irradiation to achieve self-organized nano-channel based structures at a threshold fluence of 5×10^{16} ions/cm^2 at ambient temperature is presented. Although x-ray diffraction results suggest the amorphization of as-grown TiO_2 layers, detailed transmission electron microscopy study reveals fluence-dependent evolution of voids and eventual formation of self-organized nano-channels between them. Moreover, gradual increase of TiO/Ti_2O_3 in the near surface region, as monitored by x-ray photoelectron spectroscopy, establishes the upsurge in oxygen deficient centers. The impact of structural and chemical modification on *local* RS behavior has also been investigated by current-voltage measurements in conductive atomic force microscopy, while memory application is manifested by fabricating $Pt/TiO_2/Pt/Ti/SiO_2/Si$ devices. Finally, the underlying mechanism of our experimental results has been analyzed and discussed in the light of oxygen vacancy migration through nano-channels. © *2015 AIP Publishing LLC*.
[http://dx.doi.org/10.1063/1.4936961]

I. INTRODUCTION

Exponential increase in world's technological information and high speed computation[1] demands next generation non-volatile memory devices with enhanced data storage density and speed in conjunction with good endurance and retention.[2] To meet the requirements, resistive switching (RS)-based nanoscale memory devices have emerged as one of the potential candidates that work with the electric field-induced SET (i.e., switching to low resistance state, LRS) followed by a complementary RESET process (i.e., switching from LRS to high resistance state, HRS).[3] Among various materials such as metal-oxides,[2] chalcogenides,[4] and carbon-based materials,[5,6] transition metal-oxides (TMO) have extensively been investigated for developing RS devices and also for understanding the underlying mechanisms[3,7,8] in the light of electric field-induced formation of conducting filaments (CF) by oxygen vacancy (OV) migration,[9] phase change,[10] electrochemical metallization,[11] charge trapping/detrapping,[12,13] and Schottky barrier modulation.[14]

In metal/TMO/metal heterostructure-based RS devices, OVs are naturally formed in the TMO layers during thin film deposition processes and hence OV-based switching mechanisms are frequently invoked.[15] The formation of vacancies are greatly influenced, manipulated, and controlled by different deposition or preparation techniques and conditions, leading to oxygen-deficient layers like metal/MO_x/MO_{1-x}/metal, etc.[16] In this respect, TiO_2 has extensively been explored from the inception of the RS devices. Although, till now several approaches have been made, including a recent one showing the introduction of oxygen deficiencies in sputter deposited TiO_2 layers via change in oxygen partial pressure.[15] However, most of them are lacking depth-dependent control over OVs. Therefore, it is important to perform a systematic study to control the formation of OVs as a function of depth. Ion implantation (compatible with current Si technology)[17–19] technique is a powerful method for creating such depth-dependent defects by dislodging atoms, especially oxygen atoms in the active TiO_2 layer in a controlled way with the help of a suitable low energy ion beam. In fact, it was shown that ion beam technique can also be used for creating an oxygen-gradient layer in the MO matrix, and in turn introducing RS effect.[20]

In this article, we show how 50 keV Ar^+-ions can introduce depth-dependent OVs in TiO_2 layers and achieve the local RS property. We further show how the structure is amorphized by ion irradiation, while microstructural study shows an evolution of fluence-dependent voids and self-organized OV gradient nano-channels in TiO_2 layers, especially between voids at 5×10^{16} ions/cm^2. This is further corroborated with x-ray photoelectron spectroscopy (XPS), demonstrating gradual development of TiO/Ti_2O_3 near the surface with increasing ion fluence. Finally, we will show how such surface oxygen-deficient layer and nano-channels together can bring the local RS phenomenon, evidenced by conductive atomic force microscopy (*c*-AFM), and discuss it in the light of electric field driven migration of OVs through the nano-channels.

[a)]Electronic mail: aloke.kanjilal@snu.edu.in

 © 2015 AIP Publishing LLC

RIGHTSLINK

II. EXPERIMENT

To understand the RS behavior, 80 nm thick TiO_2 films were grown at room temperature (RT) on as-received Pt/Ti/SiO_2/Si substrates by 100 W RF sputtering (Excel Instruments) using a 6 mm thick 2 in. TiO_2 target (MTI corp., purity 99.99%). The substrate-to-target distance was kept at 13 cm with a substrate rotational speed of 9 rpm. The chamber base pressure was $\sim 1 \times 10^{-7}$ Torr, while the working pressure was maintained at 8 mTorr. High purity oxygen gas was purged into the chamber with a rate of 12 sccm for controlling the stoichiometry of the TiO_2 layer, while Ar (purity 99.99%) was used as a carrier gas with a flow rate of 30 sccm. Prior to TiO_2 thin film deposition, the Pt/Ti/SiO_2/Si substrates were ultrasonically cleaned with acetone followed by methanol for 10 min each.

The influences of incident ion energy and fluence in TiO_2 were studied by Tridyn,[21] while the vacancy distribution and penetration depth of ions were predicted by SRIM calculations.[22] In order to create the oxygen gradient layers in the oxide matrix, 50 keV Ar^+-ion beam was selected from these calculations. The as-grown samples were irradiated at RT under normal incidence with different fluences in the range of $(0.05–5) \times 10^{16}$ ions/cm^2. The ion beam current and ion flux were $\sim 1\,\mu$A and $\sim 6.25 \times 10^{12}$ ions/cm^2 s, respectively. It may be noted that the sample holder having thick copper block was used for irradiation and the ion flux used is much lower than that needed to rise in temperature of the sample surface; details can be found in Refs. 23 and 24. Hence, we did not cool down the thick copper sample holder (behaving as a heat sink) by water and/or LN_2 during ion irradiation by scanning the beam over an area larger than the sample for uniformity of the ion beam over the sample. The fluence is calculated per cm^2 by dividing the total dose by the actual scanned area of the ion beam. Here, the pristine sample is referred by S0, whereas the samples irradiated with fluences of 5×10^{14}, 1×10^{15}, 5×10^{15}, 1×10^{16}, and 5×10^{16} ions/cm^2 are represented by S1, S2, S3, S4, and S5, respectively.

The structural characterizations were performed by grazing-incidence x-ray diffraction, GIXRD (Bruker D8 Discover) with an incidence angle of 0.5°. Microstructures were examined by 300 keV FEI Tecnai G^2 S-Twin transmission electron microscopy (TEM) in cross-sectional geometry. Surface chemical analyses were carried out using Mg-K_α (wavelength = 9.89 Å) source in an XPS system (VSW Ltd., UK) integrated with a hemispherical analyzer of radius $\sim$150 mm, attached in a gas aggregation type nanocluster deposition system.[25] The base pressure in the XPS chamber was 5×10^{-10} mbar and during experiment vacuum was maintained at 5×10^{-9} mbar. Since atomic force microscopy (AFM) and its complimentary *c*-AFM are known to be powerful tools to examine the grains and local electrical properties,[26,27] surface morphology and current mapping have also been studied by Park XE-7 in both AFM and *c*-AFM modes, respectively.[7,28,29] For investigating the RS behavior locally, current-voltage (*I–V*) measurements were carried out by swiping the applied potential between the movable top electrode (i.e., conducting Pt/Ir *c*-AFM tip with radius of curvature of $\sim$40 nm) and Pt rear-contact with a current compliance of 10 nA. For device testing, standard Pt/TiO_2/Pt/Ti/SiO_2/Si memory devices have been fabricated, where the top Pt electrodes of radius $\sim$500 μm were developed by electron beam deposition using shadow masking. Initially, the *I-V* characteristics were verified using a semiconductor parameter analyzer (Kiethley-4200SCS), where the top electrode was biased by keeping the bottom electrode grounded.

III. RESULTS AND DISCUSSION

Figure 1(a) exhibits the results obtained from Tridyn calculations[21] showing the variation of titanium (Ti) and oxygen (O) atomic fractions in the TiO_2 layers of S1, S3, and S5 samples as a function of depth. In comparison to both S1 and S3, S5 shows significant decrease in Ti concentration by subsequent increase of O with increasing depth, indicating the development of near surface oxygen deficient regions with increasing fluence.[19] Such a preferential sputtering of O can be due to the relatively weak surface binding energy (2 eV) than that of Ti (4.89 eV).[18] In the inset, the exponential increase of sputtering loss of TiO_2 with increasing ion fluence is clearly visible.

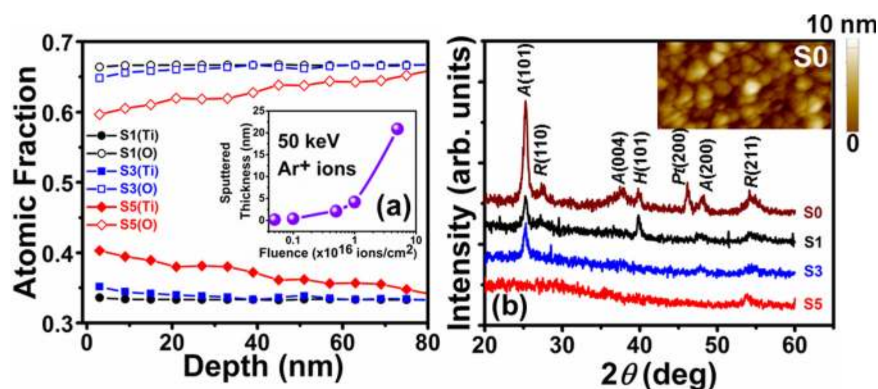

FIG. 1. (a) Tridyn results of Ar^+-ion irradiated TiO_2 layers with fluences of 5×10^{14} (S1), 5×10^{15} (S3), and 5×10^{16} ions/cm^2 (S5), showing the depth-dependent change in Ti (solid symbols) and O (open symbols) atomic fractions; inset represents the thicknesses of sputtered TiO_2 layers as a function of ion fluence. (b) GIXRD patterns before (S0) and after irradiation with fluences of 5×10^{14} (S1), 5×10^{15} (S3), and 5×10^{16} ions/cm^2 (S5); various reflections from the planes of anatase (*A*), rutile (*R*), and Ti-rich (i.e., $TiO_{0.325}$) hexagonal (*H*) phases are indicated in S0. The (200) peak from the underlying Pt layer is also presented. Typical AFM image of S0 (scan area: 1 μm × 0.5 μm) with rms roughness of $\sim$3 nm is shown in the inset where color scale bar represents the height modulation.

RIGHTSLINK

The GIXRD pattern of S0, depicted in Fig. 1(b), suggests that the development of polycrystalline TiO_2 is dominated by anatase phase (A) along with rutile phases (R) peaking at $\sim$27.5° and $\sim$54.3°, and trace amount of Ti-rich hexagonal, H(101) phase. Reflection from Pt(200) plane is also observed at $\sim$46.2° in S0 which was disappeared after exposing to ion beam [see Fig. 1(b)]. This could be due to the damaging crystallinity of the below Pt layer as is supported by SRIM calculations[22] with ion projection range beyond 80 nm (not shown). Here, the observed GIXRD peaks are marked according to the JCPDS files (03-065-5714, 00-021-1276, 01-073-1581, and 03-065-2868 for A, R, H, and Pt, respectively). Further, analysis reveals a systematic change in anatase peak intensity, especially the one originating at $\sim$25.2° with increasing fluence that eventually disappears at a fluence of 5×10^{16} ions/cm^2 due to the amorphisation of polycrystalline TiO_2 phase. The surface morphology of S0 (inset) obtained from AFM shows a granular feature with an rms roughness of $\sim$3 nm which enhances with increasing ion fluence.

Figure 2(a) shows a schematic presentation of the c-AFM measurement of the TiO_2/Pt/Ti/SiO_2/Si sample in contact mode, while the second row in Fig. 2(b) exhibits a series of c-AFM images of the top TiO_2 layers of the ion irradiated samples using a +2 V bias between the AFM-tip and the bottom Pt layers. The data from S0 are not shown here as no signal was obtained even up to +10 V. These results show that the electrical conduction across the TiO_2 layer was improved with increasing ion fluence, demonstrating a clear transformation of the insulating-to-conducting TiO_2 layers. This can be attributed to the introduction of more-and-more OVs which will serve as donors in the oxide matrix and in turn contribute to the electrical conduction. This is consistent with the results obtained from the Tridyn calculations (discussed above) and also supported by a recent report in which Ghenzi *et al.*[15] showing the contribution of OVs by converting TiO_2 into an n-type semiconductor. Although there is a clear signature [Fig. 2(b)] of increasing surface current density as a function of ion fluence up to 1×10^{16} ions/cm^2 for S4, a sudden drop is noticed in S5. To understand such intriguing phenomenon, a set of c-AFM images have also been recorded for S5 with bias voltages of 0.5, 1.0, 1.5, and 2.0 V as exhibited in the third row [Fig. 2(c)]. They clearly show rise in current density with increasing potential at only certain locations on the surface. A close inspection of Fig. 2(d) is displayed in Fig. 2(e), which reveals the corresponding surface morphology that confirms charge flow through the TiO_2 layer between insulating mounts (within cyan-dashed curves). This suggests that the conducting channels between the mounts are most likely rich in OVs facilitating the charge transport.

For further understanding the role of OVs, detailed microstructural investigations were carried out by cross-sectional TEM (XTEM). The bright-field image of S0 [Fig. 3(a)] shows the formation of columnar structure of TiO_2 with an average length of $\sim$80 nm and width in the range of 20–40 nm. Selected-area electron diffraction (not shown) and high-resolution TEM [Fig. 3(b)] of the projected column, marked by a dashed circle in Fig. 3(a), confirm the polycrystalline nature of S0, in consistent with our GIXRD results [see Fig. 1(b)]. A typical XTEM image [Fig. 3(c)] of the Ar^+-ion irradiated sample (S4) shows the disappearance of columnar structure and the formation of a large number of 3–5 nm size voids (indicated by two red arrows). An evolution of bigger voids in the range of 50–70 nm along with smaller ones is, however, observed in S5 [Fig. 3(d)]. Clearly, the appearance of bigger voids can be attributed to the coalescence of smaller ones at a fluence of 5×10^{16} ions/cm^2. The formation of such giant voids makes the surface rough and thus producing mount-like insulating structure as is also seen during the AFM analysis [Fig. 2(e)].

Since the stoichiometry plays an important role in charge transport, the composition of the TiO_2 layer was monitored by energy-filtered TEM (EFTEM). The magnified EFTEM images of S0 and S5 are presented in Figs. 3(e) and 3(f), respectively. Comparing these EFTEM images, it is revealed that the TiO_2 layer in S5 swells at those places where bigger voids are formed and thus make these regions non-conducting, in agreement with the results obtained from c-AFM studies [Fig. 2(c)]. Looking at the Ti M-edge in S5

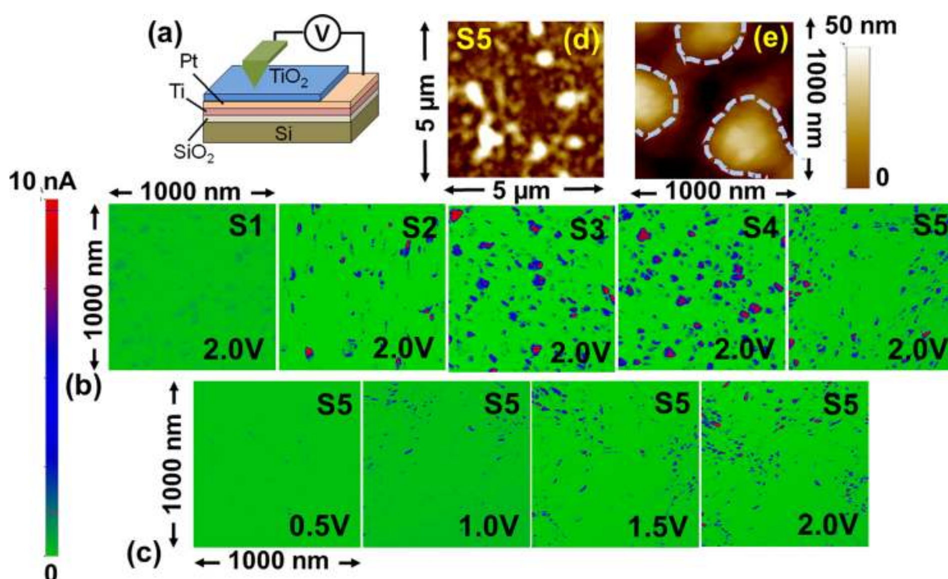

FIG. 2. (a) Schematic diagram of c-AFM experiments on TiO_2/Pt/Ti/SiO_2/Si where the Pt/Ir tip in c-AFM acting as a movable top electrode; (b) second row exhibits the c-AFM images (scan area: 1 μm $\times$ 1 μm) for all the ion irradiated samples, namely, S1 to S5, at +2 V bias in the Pt back electrode; (c) third row presents current maps of the TiO_2 surface for a systematic increase in sample bias from 0.5 to 2 V. Typical surface morphology of S5 with rms roughness of $\sim$17.3 nm is shown in (d) with a scan area of 5 μm $\times$ 5 μm, while the magnifying view in (e) with a scan area of 1 μm $\times$ 1 μm shows the region in which current maps were acquired; the cyan dashed curves in (e) are representing the insulating mounts.

RIGHTSLINK

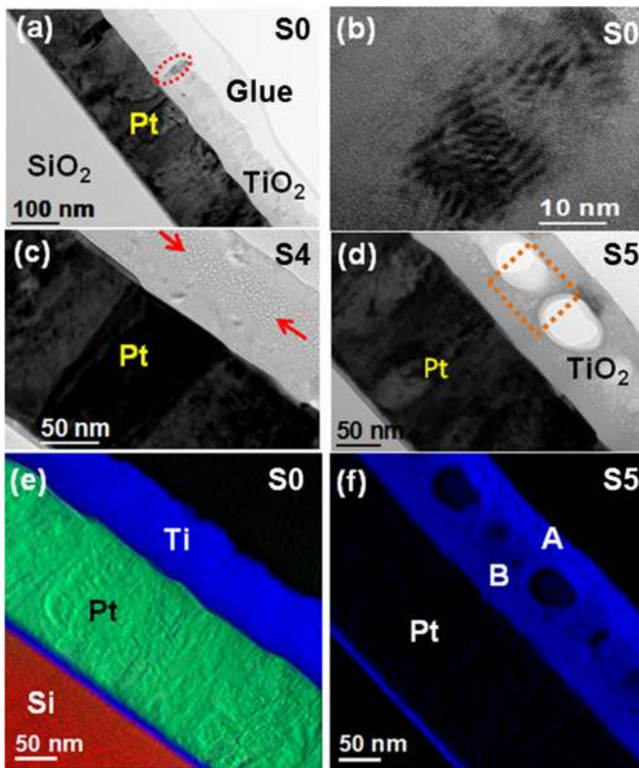

FIG. 3. (a) Bright-field XTEM image of S0; (b) HRTEM image of S0 taken from the dashed red circled region in (a); XTEM images of S4 in (c) showing smaller size voids in TiO_2 indicated by two red arrows where (d) shows the formation bigger voids in S5. The dashed rectangle in (d) represents a nano-channel region. EFTEM images of S0 and S5 are depicted in (e) and (f), respectively. The blue, green, and red color indicates the data collected from Ti-*M*, Pt-*O*, and Si-*L* edges, respectively [except in (f) for Pt, showing only the locations]. Maximum and minimum oxygen deficient regions along the oxide nano-channel are indicated by A and B, respectively.

[Fig. 3(f)], one can see that the surface region (indicated by A) is more Ti-rich than that of the deeper depth (indicated by B). From these results, it can be inferred that this oxygen concentration gradient as a function of depth is responsible for the variation in resistivity (or conductivity) of the channels.

For further confirmation of the surface sub-oxide layer formation, surface chemical properties have been investigated by XPS. The Ti-2*p* spectra of TiO_2 films were acquired before and after irradiation with different fluences. Here, we are displaying typical spectra recorded from S0 and S5 (see Fig. 4), showing the evolution of Ti_2O_3 (Ti^{3+}) phase [with a possible contribution from TiO (Ti^{2+})][30] from pure TiO_2 (Ti^{4+}) in the former case, as is revealed by deconvoluting those spectra with the help of Voigt function (70% Gaussian and 30% Lorentzian) after Shirley-type background subtraction (Ref. 17 and references therein). However, an insignificant modification of the spectrum was observed up to S3 (fluence: 5×10^{15} ions/cm^2), while the evolution of TiO/Ti_2O_3 was noticed with increasing fluence as the one shown for S5. The possible existence of such mixed sub-oxide phases could be responsible for increasing full-with at half maximum. The detailed analyses, in particular, reveal that Ti-2$p_{3/2}$ and Ti-2$p_{1/2}$ peaks are originated at 459.31 and 465.01 eV, respectively, in S0, in agreement with the previous reports.[30,31] However, two additional sub-oxide peaks

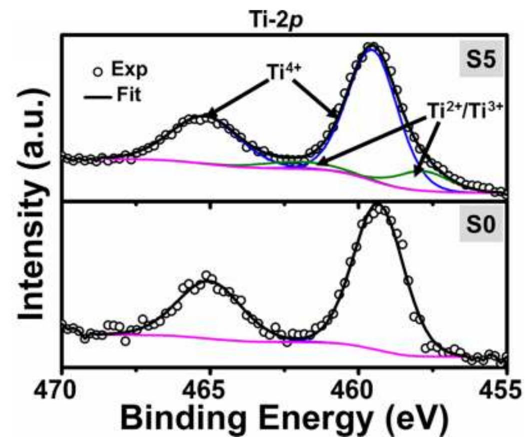

FIG. 4. Ti-2p core level XPS spectra of TiO_2 before Ar^+-ion irradiation (S0) and after irradiation with a fluence of 5×10^{16} ions/cm^2 (S5) are shown. Experimental results are exhibited by open circles. Background (in magenta) subtraction and the deconvoluted curves for Ti^{4+} (in blue) and Ti^{2+}/Ti^{3+} (in green) are also shown along with the fitted curve (in black).

are observed in S5 at binding energies of 457.8 and 462 eV.[31] These two peaks are originated due to the formation of oxygen deficient TiO/Ti_2O_3 surface layer by deteriorating the stoichiometry of TiO_2,[30,32] with a maximum atomic concentration of ~13.66%. These results suggest bombardment with energetic ions leads to the formation of oxygen vacancy-rich layer at the top of TiO_2 in S5 which is in consistent with our TEM results shown in Fig. 3. Using the complementary *I-V* characteristics under *c*-AFM, we will now show how such variation in O concentration along the TiO_2 nano-channels helps to achieve nanoscale RS behavior.

Figure 5(a) shows the local I-V characteristics of selected samples S1, S3, and S5 in linear scale using a compliance current (I_c) of 10 nA. The result of S0 is not shown here due to its insulating nature, though the RS behavior is merely observed in S1 by swiping potential between ±2 V. However, the increasing ion fluence can lead to a significant change in the hysteresis loop that in turn gives a prominent memory window for S5 without applying any forming potential. In particular, the hysteresis loop of S5 offers a bi-stable property within ±1V. The direction of the hysteresis loops are also indicated by arrows. For detailed understanding, *I-V* characteristics is plotted again in semi-log scale, as shown in Fig. 5(b), where one can see that the crossing potential (V_c) moves from about −0.8 to −0.1 V with increasing fluence up to 5×10^{16} ions/cm^2 (marked by an right arrow). This non-zero V_c can be attributed to the parasitic inductive contribution in the present devices.[33] Moreover, the observed shifting of V_c towards first quadrant can be associated with the increasing contribution of dynamic parasitic capacitance with increasing ion fluence.[33]

In order to explore further, the region around V_c for S5 is magnified as the one shown in Fig. 5(c). The key finding is that the V_c for the forward and reverse directions (indicated by thinner arrows) are not coinciding and as a consequence it gives rise to a negative voltage shift of ~0.25 V (shown by left thicker arrow). Although this phenomenon has previously been observed[34] but not adequately understood. Since the shift in V_c is known to be governed by the change in

RIGHTSLINK

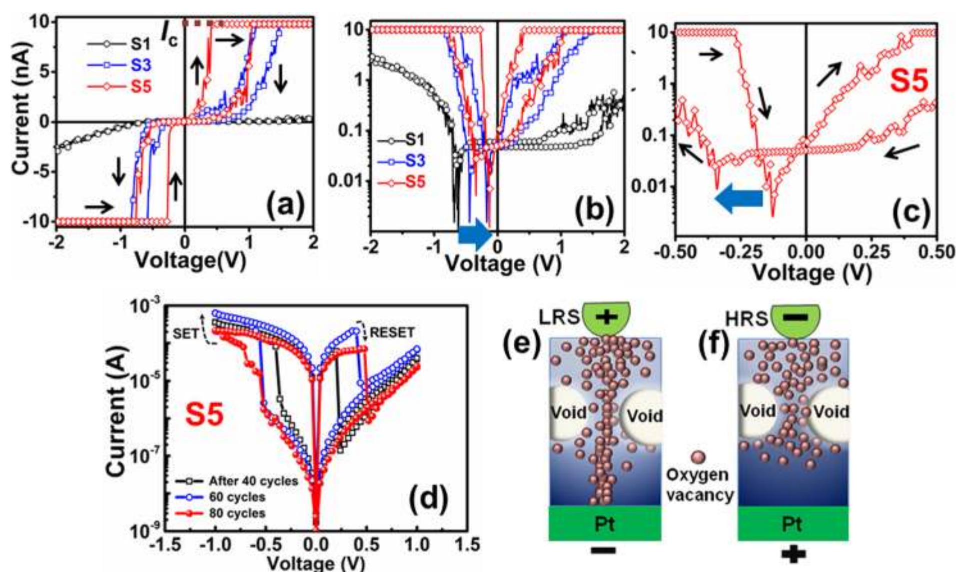

FIG. 5. (a) Local *I-V* characteristics of S1 (open circles), S3 (open squares), and S5 (open diamonds) by sweeping the applied potential across the AFM tip and Pt back electrode from −2 V to +2 V and back to −2 V with compliance current (I_c) 10 nA; (b) corresponding semi-log plots in (a) indicating gradual evolution of RS window with increasing fluence. Thick arrow indicates the shifting of non-zero crossing towards zero potential; (c) magnified region around crossing potential for S5, showing forward (−2 V to +2 V) and reverse (+2 V to −2 V) sweeps with negative shift, indicated by thick blue arrow; (d) *I-V* characteristics of the Pt/TiO_2/Pt/Ti/SiO_2/Si memory devices for S5 showing a self-compliance bi-stable RS behavior within ±1 V after 40 (open squares in black), 60 (open circles in blue), and 80 (filled circles in red) cycles; schematic presentation of corresponding (e) low resistance state, LRS, and (f) high resistance state, HRS, mechanisms, controlled by OV migration through changing applied electric field direction.

dynamic capacitance in the presence of a small filamentary area,[35] we believe that the phenomenon in Fig. 5(c) could be influenced by the stray capacitance at the interface between the top electrode (i.e., *c*-AFM tip) and oxide due to surface contamination under ambient condition.[36] Moreover, the observed short-circuit current is most likely associated with the screening of the injected electrons into the active oxygen deficient TiO_2 nano-channels[34] by creating a space charge region via trapping of hot electrons in vacancies and interstitials. This ultimately changes the effective potential from the applied one.

Standard Pt/TiO_2/Pt/Ti/SiO_2/Si memory devices have also been investigated to justify the above discussion. Here, the device was SET to LRS by applying a voltage of −1 V, followed by a voltage sweep to +1 V, in which it switched to HRS below +0.5 V [see Fig. 5(d)]. Interestingly, this device shows a *self-compliance* bi-stable *I-V* characteristic within ±1 V up to 80 dc cycles without any degradation; the details of the device performance will be studied later and published elsewhere. Compared with the *c*-AFM results [see Figs. 5(b) and 5(c)], here we did not observe any non-zero V_c, indicating the importance of contact area of the top electrode and the corresponding interface with the active oxide layer. Based on the TEM (Fig. 3) and XPS (Fig. 4) analyses in association with *c*-AFM results, the observed bi-stable RS behavior can be explained in the light of OV migration through nano-channels as is discussed in the following.

Based on the above findings, it is therefore clear that the ion beam induced OVs can play a dominating role in controlling the RS behavior, especially bi-stable mechanism[3,22] in the absence of forming potential. This is particularly associated with the electric field-driven back and forth OV migrations, leading to a CF formation and annihilation along the Ar^+-ion induced oxygen gradient in nano-channels.[37] The dimension of the CF depends on the OV density[15] which enhances with increasing ion fluence as observed by the microstructural and spectroscopic investigations (Figs. 3 and 4). The observed LRS and HRS are schematically exhibited in Figs. 5(e) and 5(f), respectively. During SET operation (for switching to LRS), hot electrons will flow predominantly through the conducting nano-channels under negative bias to Pt rear electrode and subsequently develops a space charge region near the top electrode as discussed in the recent literature.[37] On the other hand, during RESET operation (for switching to HRS), applied positive bias in the Pt electrode drives these OVs towards the AFM tip (top electrode), resulting the annihilation of conducting channels.[16]

IV. CONCLUSIONS

In summary, we have shown the transformation of polycrystalline to amorphous TiO_2 layers by 50 keV Ar^+-ion beam irradiation at RT in the fluence range of (0.05–5) $\times 10^{16}$ ions/cm^2 with the help of GIXRD. The formation of isolated conducting regions surrounded by insulating mounts is revealed in *c*-AFM. Detailed TEM investigations, however, suggest the evolution of nano-channels with gradient OVs below the mounts and surrounded by voids. This is also consistent with the XPS results, showing an increase of TiO/Ti_2O_3 phase near the surface as a function of ion fluence, which reaches its maximum at 5×10^{16} ions/cm^2. Using *c*-AFM, local *I-V* measurements from the nano-channels have shown the evolution of RS loops with two distinct low and high resistance states that become prominent with increasing fluence. Moreover, the existence of non-zero crossing potential (V_c) at lower fluences is attributed to the influence of both resistive and inductive effects,

RIGHTSLINK

while V_c shifts towards zero potential at higher fluences has been assigned to the increase in capacitive contribution. This is justified by fabricating two-terminal Pt/TiO_2/Pt/Ti/SiO_2/Si memory devices, followed by monitoring the *I-V* characteristics at RT. Detailed analyses suggest that the observed RS behavior can be discussed in the light of OV migration through the self-organized nano-channels. We believe that the present work will bring opportunities to develop high density nano-channel based RS devices, but it requires further optimization of the voids dimension and/or distribution for practical application.

ACKNOWLEDGMENTS

The authors, especially A.K., would like to acknowledge the financial support received from Shiv Nadar University and also from Department of Science and Technology India under Project No. DST/EMR/2014/000971. The help received from the scientists at Inter-University Accelerator Centre is acknowledged.

[1]M. Hilbert and P. López, Science **332**, 60 (2011).
[2]R. Waser, R. Dittmann, G. Staikov, and K. Szot, Adv. Mater. **21**, 2632 (2009).
[3]H.-S. P. Wong, H.-Y. Lee, S. Yu, Y.-S. Chen, Y. Wu, P.-S. Chen, B. Lee, F. T. Chen, and M.-J. Tsai, Proc. IEEE **100**, 1951 (2012).
[4]F. Zhuge, K. Li, B. Fu, H. Zhang, J. Li, H. Chen, L. Liang, J. Gao, H. Cao, Z. Liu, and H. Luo, AIP Adv. **5**, 057125 (2015).
[5]M. Rogala, P. J. Kowalczyk, P. Dabrowski, I. Wlasny, W. Kozlowski, A. Busiakiewicz, S. Pawlowski, G. Dobinski, M. Smolny, I. Karaduman, L. Lipinska, R. Kozinski, K. Librant, J. Jagiello, K. Grodecki, J. M. Baranowski, K. Szot, and Z. Klusek, Appl. Phys. Lett. **106**, 263104 (2015).
[6]C. A. Santini, A. Sebastian, C. Marchiori, V. P. Jonnalagadda, L. Dellmann, W. W. Koelmans, M. D. Rossell, C. P. Rossel, and E. Eleftheriou, Nat. Comm. **6**, 8600 (2015).
[7]M. Lanza, Materials **7**, 2155 (2014).
[8]U. Chand, K.-C. Huang, C.-Y. Huang, C.-H. Ho, C.-H. Lin, and T.-Y. Tseng, J. Appl. Phys. **117**, 184105 (2015).
[9]D. B. Strukov, G. S. Snider, D. R. Stewart, and R. S. Williams, Nature **453**, 80 (2008).
[10]J. J. Yang, M. D. Pickett, X. Li, D. A. A. Ohlberg, D. R. Stewart, and R. S. Williams, Nat. Nanotechnol. **3**, 429 (2008).
[11]S. Peng, F. Zhuge, X. Chen, X. Zhu, B. Hu, L. Pan, B. Chen, and R.-W. Li, Appl. Phys. Lett. **100**, 072101 (2012).
[12]C. Zhu, Z. Xu, Z. Huo, R. Yang, Z. Zheng, Y. Cui, J. Liu, Y. Wang, D. Shi, G. Zhang, F. Li, and M. Liu, Appl. Phys. Lett. **99**, 223504 (2011).
[13]X. Zou, H. G. Ong, L. You, W. Chen, H. Ding, H. Funakubo, L. Chen, and J. Wang, AIP Adv. **2**, 032166 (2012).
[14]J. H. Hur, M.-J. Lee, C. B. Lee, Y.-B. Kim, and C.-J. Kim, Phys. Rev. B **82**, 155321 (2010).
[15]N. Ghenzi, M. J. Rozenberg, R. Llopis, P. Levy, L. E. Hueso, and P. Stoliar, Appl. Phys. Lett. **106**, 123509 (2015).
[16]Y. H. Do, J. S. Kwak, Y. C. Bae, K. Jung, H. Im, and J. P. Hong, Appl. Phys. Lett. **95**, 093507 (2009).
[17]X. Ou, Y. Shuai, W. Luo, P. F. Siles, R. Kögler, J. Fiedler, H. Reuther, S. Zhou, R. Hübner, S. Facsko, M. Helm, T. Mikolajick, O. G. Schmidt, and H. Schmidt, ACS Appl. Mater. Interfaces **5**, 12764 (2013).
[18]H. Wylezich, H. Mähne, J. Rensberg, C. Ronning, P. Zahn, S. Slesazeck, and T. Mikolajick, ACS Appl. Mater. Interfaces **6**, 17474 (2014).
[19]B. M. Pabón, J. I. Beltrán, G. Sánchez-Santolino, I. Palacio, J. López-Sánchez, J. Rubio-Zuazo, J. M. Rojo, P. Ferrer, A. Mascaraque, M. C. Muñoz, M. Varela, G. R. Castro, and O. Rodríguez de la Fuente, Nat. Commun. **6**, 6147 (2015).
[20]W. D. Song, J. F. Ying, W. He, V. Y.-Q. Zhuo, R. Ji, H. Q. Xie, S. K. Ng, S. L. G. Ng, and Y. Jiang, Appl. Phys. Lett. **106**, 031602 (2015).
[21]W. Möller, W. Eckstein, and J. P. Biersack, Comput. Phys. Commun. **51**, 355 (1988).
[22]J. F. Ziegler, M. D. Ziegler, and J. P. Biersack, Nucl. Instrum. Methods Phys. Res., Sect. B **268**, 1818 (2010).
[23]S. Dhar, T. Som, Y. N. Mohapatra, and V. N. Kulkarni, Appl. Phys. Lett. **67**, 1700 (1995).
[24]C.-H. Lai, C.-H. Yang, and C. C. Chiang, Appl. Phys. Lett. **83**, 4550 (2003).
[25]S. Mondal and S. R. Bhattacharyya, Rev. Sci. Instrum. **85**, 065109 (2014).
[26]M. Lanza, A. Bayerl, T. Gao, M. Porti, M. Nafria, G. Y. Jing, Y. F. Zhang, Z. F. Liu, and H. L. Duan, Adv. Mater. **25**, 1440 (2013).
[27]V. Iglesias, M. Lanza, K. Zhang, A. Bayerl, M. Porti, M. Nafría, X. Aymerich, G. Benstetter, Z. Y. Shen, and G. Bersuker, Appl. Phys. Lett. **99**, 103510 (2011).
[28]Y. Du, A. Kumar, H. Pan, K. Zeng, S. Wang, P. Yang, and A. T. S. Wee, AIP Adv. **3**, 082107 (2013).
[29]M. Rogala, Z. Klusek, C. Rodenbücher, R. Waser, and K. Szot, Appl. Phys. Lett. **102**, 131604 (2013).
[30]M. J. Jackman, A. G. Thomas, and C. Muryn, J. Phys. Chem. C **119**, 13682 (2015).
[31]S. Gutmann, M. A. Wolak, M. Conrad, M. M. Beerbom, and R. Schlaf, J. Appl. Phys. **107**, 103705 (2010).
[32]R. L. Kurtz and V. E. Henrich, Surf. Sci. Spec. **5**, 179 (1998).
[33]L. Qingjiang, A. Khiat, I. Salaoru, C. Papavassiliou, X. Hui, and T. Prodromakis, Sci. Rep. **4**, 4522 (2014).
[34]P. Predeep, Dinumol Devasia, J. Aneesh, and N. M. Faseena, Microelectron. Eng. **107**, 54 (2013).
[35]B. Mouttet, arXiv:1003.2842 (2010).
[36]M. Trapatseli, D. Carta, A. Regoutz, A. Khiat, A. Serb, I. Gupta, and T. Prodromakis, T J. Phys. Chem. C **119**, 11958 (2015).
[37]D. Y. Guo, Z. P. Wu, L. J. Zhang, T. Yang, Q. R. Hu, M. Lei, P. G. Li, L. H. Li, and W. H. Tang, Appl. Phys. Lett. **107**, 032104 (2015).

RIGHTSLINK